UNIVERSITÄT ZU LÜBECK
INSTITUTE OF MATHEMATICS
AND IMAGE COMPUTING

Hermite-Birkhoff Interpolation with Radial Basis Functions for Surface Modeling

Hermite-Birkhoff-Interpolation mit radialen Basisfunktionen zur Oberflächenmodellierung

Bachelorarbeit

verfasst am
Institute of Mathematics and Image Computing

im Rahmen des Studiengangs
Mathematik in Medizin und Lebenswissenschaften
der Universität zu Lübeck

vorgelegt von
Alina Ritter

ausgegeben und betreut von
Prof. Dr. Jan Modersitzki

Lübeck, den 3. September 2025

Eidesstattliche Erklärung

Ich erkläre hiermit an Eides statt, dass ich diese Arbeit selbständig verfasst und keine anderen als die angegebenen Quellen und Hilfsmittel benutzt habe.

_____

Alina Ritter

Zusammenfassung

Eine Linearkombination von Riesz-Darstellern interpoliert Funktionswerte der zugehörigen stetigen linearen Funktionale, die nach dem Darstellungssatz von Fréchet-Riesz eindeutig zuordenbar sind. Diese interpolierende Funktion wird unter allen Funktionen, die die generierten Funktionswerte interpolieren, als Minimum bezüglich der Norm des Hilbertraums, aus dem die Riesz-Darsteller stammen, bewiesen. Dieser in der Arbeit präsentierte Interpolationsansatz wird auf die Hermite-Birkhoff-Interpolation mit radialen Basisfunktionen (RBFs) spezifiziert, indem die linearen Funktionale in Form einer Verkettung von Auswertung und Differentiation gewählt werden. Das Konzept wird dann zur Modellierung von implizit definierten Oberflächen genutzt, die durch Punkte und Normalenvektoren beschrieben werden. Im Vergleich der von Gauß und Wendland eingeführten RBFs bei der Oberflächenrekonstruktion zeigt sich, dass der freie Parameter der Gauß RBFs die Krümmung der Oberfläche beeinflusst und der Parameter der Wendlandfunktionen einen Interpolationsradius angibt. Optische Rückstände des kompakten Trägers der Wendlandfunktionen können durch die Eingliederung von Polynomtermen in die interpolierende Funktion aufgehoben werden. Die Raumerweiterung mit Polynomen im Allgemeinen hat einen optisch glättenden Effekt in den Oberflächen.

Abstract

A linear combination of Riesz representers interpolates values generated by the evaluation of the associated continuous linear functionals. The interpolant of that form is proven to be norm-minimal among all functions interpolating the generated values in the Hilbert space containing the Riesz representers. This in the thesis displayed interpolation approach is specialized to Hermite-Birkhoff interpolation with radial basis functions (RBFs) by choosing a composition of evaluation and differentiation as linear functionals. The interpolation framework is then applied to the problem of modeling surfaces implicitly through a function that interpolates given data, i.e. points and normal vectors. Comparing Gaussian and Wendland RBFs in the interpolation for surface modeling, Gaussian's shaping parameter influences the surface curvature whereas Wendland's denotes an interpolation radius. Optical traces of the Wendland RBF's compact support are revoked by including a polynomial term into the interpolating function. The augmentation with polynomials in general evokes an optical smoothing in the surfaces.

Acknowledgements

I especially thank my superviser Jan Modersitzki who patiently adviced me throughout the formation process of this thesis. My gratitude goes also to Amanda and Adrian for their support.

Contents

1

Introduction

For geometric modeling it is possible to receive object-related data, for example with a laser scanner, to reconstruct that object's surface; cf. [10]. The surface can be described by creating a polygon mesh or by interpolating a function based on the related data. Interpolation is a method in numerical analysis for building a function, which runs through the given data points, that are given function values mapped from nodes on a mesh. Since the nodes of scanned interpolation data might not lie on a regular mesh (also referred to as "scattered data"), meshless interpolation techniques are required in this setup; cf. [10]. Interpolation with radial basis functions is an already widely established method for this problem, as they work reliably on irregular data distributions; cf. [4].
A radial basis function (RBF) is a translation- and rotation-invariant function that depends primarily on the norm of its argument. Additionally, the function can be centered at a point other than zero so that the normed distance of the argument to that center is evaluated. An interpolating function, within this thesis called interpolant, can be constructed by linearly combining all nodes as center of such a radial basis function with specific real coefficients; cf., e.g. [7]. These coefficients can be determined by solving linear equations that form through mapping every node by the interpolant and matching the result to the corresponding given function values. Summarizing this to one linear equation system also delivers the so-called interpolation matrix. In addition to this interpolation approach there also exists a concept for not only interpolating function values but also derivative values – the Hermite interpolation; cf., e.g.[7]. Its extension – Hermite-Birkhoff interpolation – even allows to interpolate values of derivatives of non-successive order at a node, cf. [10]. The Hermite-Birkhoff interpolation and the interpolation with radial basis functions can not only be combined but also be generalized to an abstract concept that interpolates linear functionals of a Hilbert space's continuous dual space.
Surfaces can be implicitly described by a function on spatial points whereby its zeros define the set of points belonging to the surface [2]. It is known that the gradient of such a function is equal to the normal vector at the same point. Therefore, Hermite-Birkhoff interpolation with RBFs can be utilized to reconstruct a surface that is defined through a point cloud with associated normal vectors. This concept can be applied in medical imaging, for instance in the production of cranial implants [4].

1.1 Related Work

Multivariate interpolation works especially well with concepts relying on RBFs. These concepts provide a quite simple approach to data non lying on a regular mesh; cf. [7]. Wendland authored an opus for scattered data interpolation [10] and also unified numerical aspects of multivariate interpolation and approximation in his summary [11]. Deducing a linear combination of radial basis functions as solution for the interpolation problem can follow through the reproducing kernel Hilbert spaces theory and the representer theorem from statistical learning [1] or solving a variational problem and constructing representers therein [6]. A vast input to the first order Hermite-Interpolation has been contributed by the field of computer graphics. Its interpolation's purpose is to model a surface determined by only one function and described through a point cloud and associated normal vectors. The normal vector at a point can be estimated from local neighborhood points; cf. [3]. Its incorporation into the interpolant is imperative in order to avoid trivial zero interpolants and can be designed differently. Carr constructs offset points in [3] that are assigned a non-zero value to determine that they are not included in the set of points belonging to the surface. In [8] the offset points are avoided by solving a regularized variational problem, aligning normals with the interpolant's gradients. Macêdo at al. used the generalized interpolation theory by Wendland to interpolate the normals [2]. In particular, they resort to Wendland's RBF in graphical tests for surface interpolation in [2] and demonstrated the ability of the interpolation concept to handle close sheets and non-uniform distributed data.

1.2 Contributions of this Thesis

In their paper [2] Macêdo, Gois and Velho present an interpolation framework for surface modeling purposes, which is strongly influenced by the work of Wendland [10]. In this thesis, the aforementioned multivariate interpolation approach is unraveled through amendments of the work provided by Wendland.
Following up and confirming a surface reconstruction example from [2], the behavior of the approach of [2] on simple solids is examined further below. Macêdo et al. used a specific radial basis function in [2], called Wendland RBF, with a compact subset of its codomain containing non-zero values, the so-called compact support. Since different radial basis functions influence the surface appearance between the data points – the interpolation's working area – differently, the behavior of the Gaussian RBF, which does not have compact support, will be studied for comparison, in addition to the Wendland RBF. Another property of the latter is "isosurfacing artifacts", which are improperly appearing surface parts; cf. [2]. Even though these artifacts are endeavored to be eliminated in computer graphics, a special interest will be placed on their characteristics, which were also included in the studies in Chapter 5.
It will be confirmed by two influencing components that the interpolation concept works well for the application of surface reconstruction: A shaping parameter in the RBFs corresponds to the surface curvature for Gaussian RBFs and represents the interpolation radius around

the data sites in the Wendland RBF case. Adding a polynomial term to the interpolant translates into a smoothing of the object's surfaces – in particular, a rounding of edges and a denting of corners – and eliminates the artifacts caused by Wendland RBFs as long as the object's surface is closed.

1.3 Structure of this Thesis

Radial basis functions are a fundamental element in this interpolation approach and appear throughout the entire thesis. Hence, a thorough understanding of them is crucial for comprehending the subsequent chapters, so the second chapter opens with a more detailed insight into RBFs. The two different kinds of RBFs to be examined – Gaussian and Wendland RBFs – are also presented therein.
Hereafter, the content is subdivided into a theoretical chapter dealing with the interpolation framework from a mathematical point of view and another chapter presenting an application from the field of computer graphics for which Macêdo et al. originally provided this concept – the interpolation of surfaces.
After presenting a general interpolation problem regarding linear functionals of a Hilbert space's dual space in Section 3.1 and the solution to it in Section 3.2, this framework is applied to the more particular case of Hermite-Birkhoff interpolation based on positive definite reproducing kernels in Section 3.3. In this case the linear functionals become a composition of an evaluation functional with a differential operator. The radial basis functions fit as an example for the kernels and thereby complete the outlined interpolation concept. Augmenting the space in which the interpolant is sought with a finite-dimensional function space as an additional modifier closes the third chapter.
Before implementing the theoretical interpolation concept for the surface reconstruction example of application, Chapter 4 begins with an excursion into modeling surfaces for the production of cranial implants. In Section 4.1 the concept of offset points is explained more thoroughly to capture the full advancement of the approach in [2]. After assembling the interpolation matrix and the interpolant in Section 4.2, some graphical tests on the interpolation concept are reviewed in Chapter 5, which take the following structure: Primarily the observations are sectioned between the Gaussian RBF in Sec. 5.1 and the Wendland RBF in Sec. 5.2 and subordinately the influence of each function is studied by the reconstruction of a cube's and a regular tetrahedron's surface. At last in Section 5.3 the two radial basis functions are compared by means of their behavior in surface interpolation.

2

On Radial Basis Functions

Radial basis functions (**RBF**s) find frequent use in scattered data interpolation and approximation for their good results even on non-regular grids and large data-free regions; cf. [4]. To understand the below explained concepts and the RBF's influence in the graphical application examples a more thorough introduction is given in the following.
Throughout this thesis let $n \in \mathbb{N}$ denote the spatial dimension and $L \in \mathbb{N}$ an arbitrary number of interpolation data.
First, there are to present the basis functions for this interpolation approach:

Definition 2.1 (radial function, cf. [7]). A function $\phi : \mathbb{R}^n \to \mathbb{R}$ is said to be radial regarding Euclid's norm $\|\cdot\|_2$ on $\mathbb{R}^n$ if there exists a corresponding function $\psi : \mathbb{R}_{\geq 0} \to \mathbb{R}$ with $\phi(\mathbf{x}) = \psi(\|\mathbf{x}\|)$ for any $\mathbf{x} \in \mathbb{R}^n$.
The radial function ϕ is said to be positive definite if the matrix $A = (\phi(\mathbf{x}^j - \mathbf{x}^k))_{j,k=1}^{L}$ is positive definite for all $\mathbf{x}^1, \ldots, \mathbf{x}^L \in \mathbb{R}^n$.

Remark 2.2. "Radial" names the direction of a circle's center point to its boundaries. Given Euclid's norm and $n = 2$ the radial function evaluates all points equally which are located on a circle line for they have equal distance to zero (compare Figure 2.1 on the following page).
Given $z \in \mathbb{R}^n$ the radial function $\phi(\cdot - \mathbf{z})$ is located at the center $\mathbf{z}$ which translates for the two-dimensional example into a translation of the circle and the circle center. This translation is depicted in the example in Figure 2.1 where $\phi_{\mathbf{z}}$ accords to ϕ translated by $(2.5, 2)^T$. Obviously, the radial functions and thereby RBFs, that are assumed to be radial regarding Euclid's norm further on, are translation invariant.

Examples 2.3 (Gaussian RBF and Wendland RBF). A radial basis function used as interpolation means in Chapter 5 is the positive definite Gaussian RBF. **Gaussian RBFs** $\phi_\varepsilon : \mathbb{R}^n \to \mathbb{R}$ accord to the formula

$$\phi_\varepsilon(\mathbf{x}) = e^{-(\varepsilon\|\mathbf{x}\|)^2}$$

where $\varepsilon > 0$ denotes a shaping parameter which can be considered as "energy" in the spline context. Gaussians are applicable on any spatial finite dimension and present no restriction on the nodes for interpolation (compare [4] including a summarizing table of characteristics concerning several RBFs). On the downside they are globally supported which leads into computational complexity for larger data sets. As one can see in Figure 2.2 on page 7 the Gaussians turn out "pointier" in $(0, 0)^T$ and appear more planar with growing radial

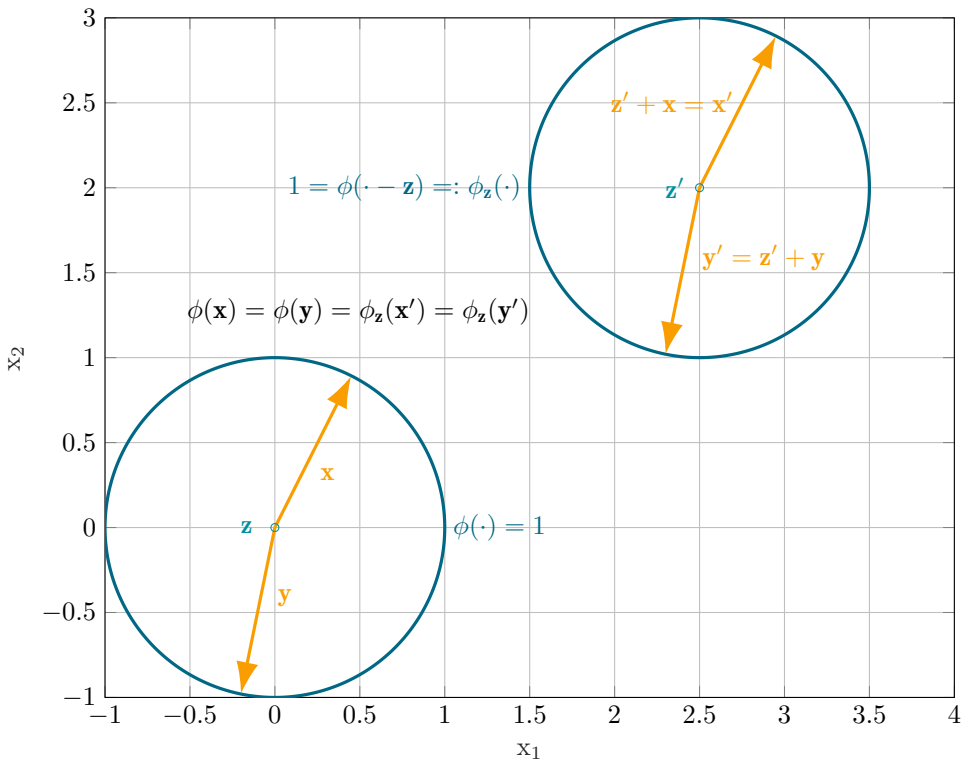

Figure 2.1: A radial function $\phi : \mathbb{R}^2 \to \mathbb{R}$ evaluates the same on vectors with norm equal to the same circle's radius. Centering ϕ in $\mathbf{z}' = (2.5, 2)^T$ instead of $\mathbf{z} = (0, 0)^T$ effects a translation of the center and the circle line, but the radial function $\phi(\cdot - \mathbf{z})$ evaluates the same on the translated $\mathbf{x}' \in \mathbb{R}^2$ and $\mathbf{y}' \in \mathbb{R}^2$. As a conclusion radial functions are translation invariant and their value just depends on the norm of their argument.

distance while increasing ε. One can also see the latter curvature behavior away from the interpolation nodes in dependence of the shaping parameter in Chapter 5.

Another kind of frequently employed RBFs use the Wendland functions $\psi_{n,q} : \mathbb{R}_{\geq 0} \to \mathbb{R}$ whose radial basis functions are in $\mathcal{C}^{2q}(\mathbb{R}^n)$, $q \in \mathbb{N}_0 := \mathbb{N} \cup \{0\}$; cf. [9]. One specific **Wendland RBF** fitting to the later graphical example is ϕ_ε with

$$\phi_\varepsilon(\mathbf{x}) := \psi_{3,1}\left(\frac{\|\mathbf{x}\|}{\varepsilon}\right) \qquad \text{for } \varepsilon > 0, \text{ using } \psi_{3,1}(t) = \frac{1}{20}(1-t)_+^4(4t+1)$$

for $t \geq 0$ with the truncated power function

$$\psi_4(t) := (1-t)_+^4 = \begin{cases} (1-t)^4, & \text{for } 0 \leq t < 1, \\ 0 & \text{for } t \geq 1 \end{cases}$$

as presented in [9]. Because of its smoothness it is hardly noticeable in the plots of Figure 2.2 on the following page that this function actually has only a compact subset in its domain not being mapped to zero – a function property commonly referred to as compactly supported. Thus, the for $\psi_{3,1}$ presented formula also demonstrates that ε is responsible for stretching and compressing the support interval $[0, 1]$ of the radial function. Compactly supported RBFs lead to more efficient algorithms for interpolation due to sparse interpolation matrices and also follow the principle of locality known from B-Splines; cf. [9]. Note that contrasting to Gaussian RBFs, Wendlands' turn out pointer in $(0, 0)^T$ with lower epsilon and the curvature behavior within the support for growing radial distance can again be recognized in the graphical examples in Chapter 5.

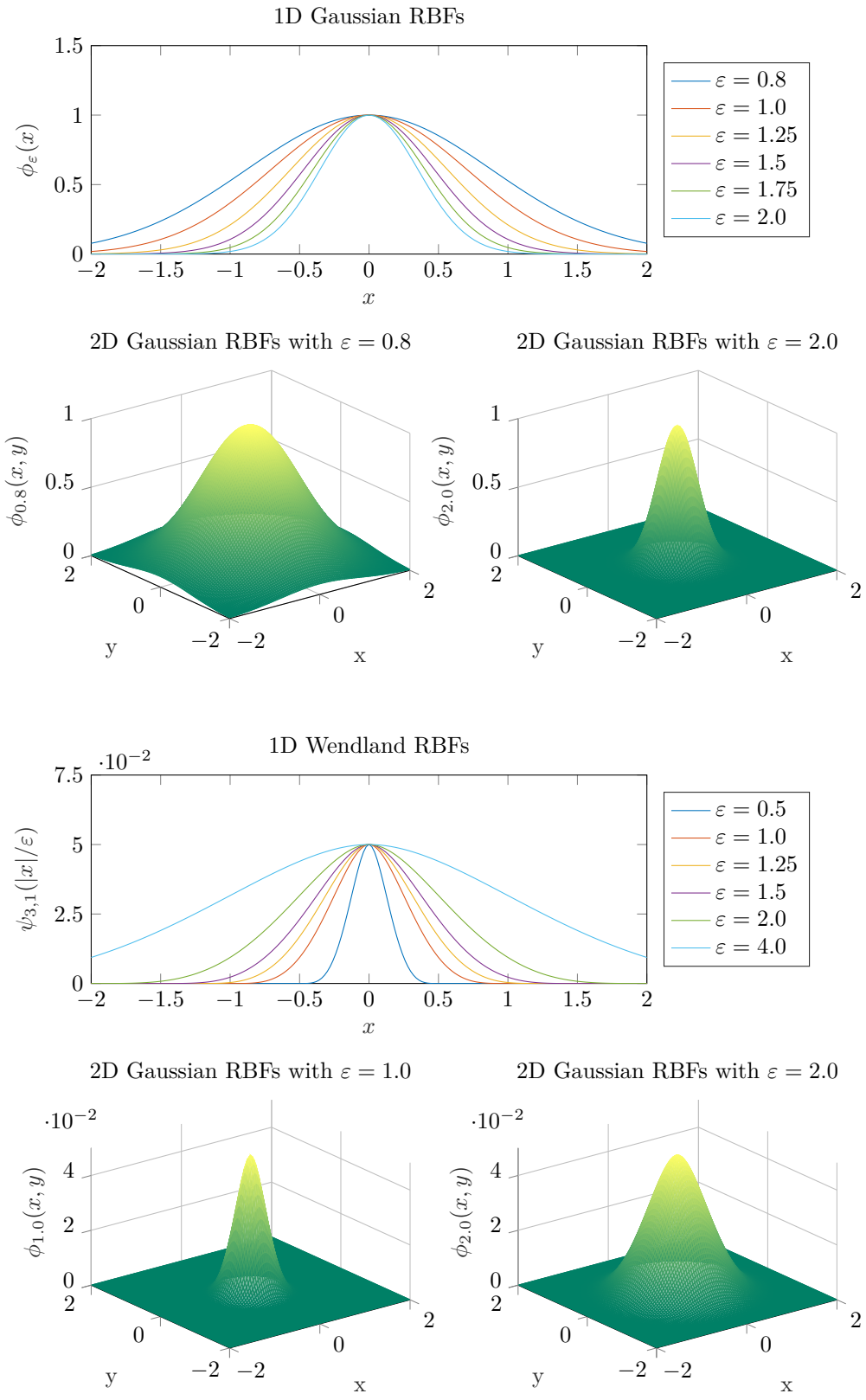

Figure 2.2: Gaussian and Wendland RBFs on $\mathbb{R}$ and $\mathbb{R}^2$ are plotted with different shaping parameters $\varepsilon > 0$.

3

Theoretical Interpolation Framework

To provide the graphical examples in Chapter 4 with a solid interpolation approach, this chapter deals with finding a solution for the general interpolation problem presented in Section 3.1. In Sections 3.2 and 3.3 a solution to it and a concept combining Hermite-Birkhoff interpolation with radial basis functions is presented. In the last part of this chapter, the space of the interpolant being sought in is augmented with a finite-dimensional function space granting its reproduction in the interpolation process.
The subsequent approach was presented in [2] and is here supplemented by the results contained in [10] due to the influence of this monograph alluded by the authors of [2] themselves.

3.1 General Interpolation Problem

Problem 3.1. Let $\mathcal{H}$ denote a real Hilbert space with inner product $\langle \cdot, \cdot \rangle_{\mathcal{H}} : \mathcal{H} \times \mathcal{H} \to \mathbb{R}$ and let $\mathcal{H}^*$ be the corresponding dual space to $\mathcal{H}$, containing all continuous linear functionals. Given $L \in \mathbb{N}$ linear independent functionals $\lambda_i \in \mathcal{H}^*$ and values $c_i \in \mathbb{R}$, $i \in 1, \ldots, L$, it is to be searched for the norm-optimal interpolant f in $\mathcal{H}$ which solves the following optimization problem:

$$\min_{u \in \mathcal{H}} \|u\|_{\mathcal{H}} \qquad s.t. \quad \lambda_i(u) = c_i, \quad \text{for all } i = 1, \ldots, L. \tag{3.1}$$

Remark 3.2. The Equation 3.1 is in [10] referred to as "optimal-recovery problem". The equations $\lambda_i(u) = c_i, \forall i \in 1, ..., L$ are further on named "interpolation conditions" in this chapter. Any function $u \in \mathcal{H}$ meeting the interpolation conditions is called a generalized interpolant (compare also [10]).

3.2 Solution of the General Interpolation Problem via Riesz Representers

As stated by the Riesz representation theorem, every continuous linear functional $\lambda_i \in \mathcal{H}^*$ has an according Riesz representer $\nu^i \in \mathcal{H}$, such that for every $i \in 1, ..., L$ and $h \in \mathcal{H}$ the equation $\lambda_i(h) = \langle \nu^i, h \rangle_{\mathcal{H}}$ holds.

Theorem 3.3. *Given the conditions from problem 3.1 with the to λ_i according representers $\nu^i \in \mathcal{H}$, the norm-optimal interpolant f takes the form*

$$f = \sum_{i=1}^{L} \mu_i \nu^i \tag{3.2}$$

with coefficients $\mu_i \in \mathbb{R}$ determined by the interpolation conditions from Eq. (3.1).

The interpolant fulfills the interpolation conditions by construction which can be seen in the computation of the coefficients μ_i hereafter; also proving the existence of such an interpolant. The norm-optimal property of f is displayed in an elegant proof by Wendland in [10] whose central idea can be formalized as follows:

Proof. It can be shown that every $h \in \mathcal{H}$ annihilated by all the linear functionals λ_i, i.e. $\lambda_i(h) = 0 \ \forall i \in \{1, \dots, L\}$, entails $\langle f, h \rangle_{\mathcal{H}} = 0$.
Assume that $u \in \mathcal{H}$ is a generalized interpolant, i.e. $\lambda_i(u) = c_i, \ \forall i \in 1, ..., L$. Then the subsequent holds:

$$\begin{aligned} \|f\|_{\mathcal{H}}^2 &= \langle f, f - u + u \rangle_{\mathcal{H}} && (3.3) \\ &= \langle f, f - u \rangle_{\mathcal{H}} + \langle f, u \rangle_{\mathcal{H}} && (3.4) \\ &= \langle f, u \rangle_{\mathcal{H}} \qquad\qquad \leq \|f\|_{\mathcal{H}} \|u\|_{\mathcal{H}}. \end{aligned}$$

In line (3.3) there is simply added a zero in the inner product. Recall in (3.4) that the **linear** functionals λ_i evaluate the same on f and u since both are meeting the interpolation conditions. Hence using the implication from the beginning with $h := f - u$, the first inner product in (3.4) is zero. Concludingly the interpolant f of form (3.2) is smaller in norm than any other generalized interpolant u. □

Using the knowledge about the shape of f from equation (3.2) - the subordinal criteria are transferred into a linear equation system by inserting f into the interpolation conditions. Thus, the problem is assembled as follows:

$$A\boldsymbol{\mu} = \mathbf{c}$$

where $A = \left(\langle \nu^j, \nu^k \rangle_{\mathcal{H}}\right)_{j,k=1}^{L}$ and with with $\boldsymbol{\mu}$ and $\mathbf{c} \in \mathbb{R}^L$ containing the coefficients μ_i respectively the given data values c_i. Obviously, the designated $A \in \mathbb{R}^{L \times L}$ is a gram matrix regarding the inner product of the set of Riesz representers. Ergo, the symmetry and positive semi definiteness are naturally granted. Further it follows that as long as the λ_i are linear independent, A is also positive definite.

3.3 Hermite-Birkhoff Interpolation Combined With Radial Basis Functions

For specifying the abstract interpolation concept from the last section on Hermite-Birkhoff-Interpolation introducing reproducing kernel Hilbert spaces respectively native spaces for positive definite kernels is necessary. Further on let Ω denote an open subset of $\mathbb{R}^n$.

Definition 3.4 (Reproducing Kernel, [10]). Let $\mathcal{H}$ be a real Hilbert space of functions $h : \Omega \to \mathbb{R}$. A function $\Phi : \Omega \times \Omega \to \mathbb{R}$ is called reproducing kernel for $\mathcal{H}$ if

1. $\Phi(\cdot, \mathbf{y}) \in \mathcal{H}$ for all $\mathbf{y} \in \Omega$,
2. $h(\mathbf{y}) = \langle h, \Phi(\cdot, \mathbf{y}) \rangle_{\mathcal{H}}$ for all $h \in \mathcal{H}$ and for all $\mathbf{y} \in \Omega$.

$\mathcal{H}$ then designates a reproducing kernel Hilbert space (**RKSH**).

Definition 3.5 ([10]). Let $\mathcal{T}$ be a group of transformations $T : \Omega \to \Omega$. Then the RKSH $\mathcal{H}$ is invariant under the group of $\mathcal{T}$ if

1. $h \circ T \in \mathcal{H}$ for all $h \in \mathcal{H}$ and for all $T \in \mathcal{T}$ and
2. $\langle g \circ T, h \circ T \rangle_{\mathcal{H}} = \langle g, h \rangle_{\mathcal{H}}$ for all $g, h \in \mathcal{H}$ and for all $T \in \mathcal{T}$.

This invariance property of the function space is inherited by its kernel.
A continuous kernel Φ is called positive definite on Ω if the matrix $(\Phi(\mathbf{x}^j, \mathbf{x}^k))_{j,k=1}^{L}$ is positive definite for any set $\{\mathbf{x}^1, \ldots, \mathbf{x}^L\} \subseteq \Omega$.

For a symmetric positive definite kernel $\Phi : \Omega \times \Omega \to \mathbb{R}$ the Native space $\mathcal{H}_\Phi(\Omega)$ is a Hilbert space of real-valued functions on Ω, induced by the span of $\{\Phi(\cdot, \mathbf{y}) : \mathbf{y} \in \Omega\}$, and Φ is its reproducing kernel. If $\Omega = \mathbb{R}^n$ and the kernel $\Phi \in \mathcal{C}(\mathbb{R}^n) \cap L_1(\mathbb{R}^n)$ is translation invariant, $\mathcal{H}_\Phi(\Omega)$ is a RKSH consisting of smooth functions. These past assertions are just a summary of the RKSH theory to be found with proofs in [10].
Turning now towards the Hermite-Birkhoff interpolation, the subsequent definitions prepare the way for concluding examples of use:

Definition 3.6. 1. Let $\boldsymbol{\eta} \in (\mathbb{N}_0)^n$ be a multiindex. $D^{\boldsymbol{\eta}} := \partial_1^{\boldsymbol{\eta}_1} \cdots \partial_n^{\boldsymbol{\eta}_n}$ designates a differential operator that maps a sufficiently smooth function onto its derivative with respect to each component according to the entry of the related coefficient of $\boldsymbol{\eta}$.
2. For $\mathbf{x} \in \mathbb{R}^n$ the operator $\delta_{\mathbf{x}} : \mathcal{C}(\mathbb{R}^n) \to \mathbb{R}$ presents an evaluation functional such that $\delta_{\mathbf{x}}(h) = h(\mathbf{x})$ for h being continuous.

Example 3.7. For $n = 3$, $\boldsymbol{\eta} = (3, 0, 2)^T$ and a sufficiently smooth function $h : \mathbb{R}^3 \to \mathbb{R}$ applying $D^{\boldsymbol{\eta}}$ on h translates into $D^{\boldsymbol{\eta}} h = \frac{\partial^5 h(x_1, x_2, x_3)}{\partial x_1^3 \partial x_3^2}$.

Remark 3.8. Let $|\boldsymbol{\eta}| := \sum_{k=1}^{n} \eta_k$ for an $\boldsymbol{\eta} \in (\mathbb{N}_0)^n$ and let $\mathbf{x}^j \in \mathbb{R}^n$ and $\boldsymbol{\eta}^j \in (\mathbb{N}_0)^n$, $j = 1, \ldots, L$, be given nodes respectively multiindices. In this Section for $q \in \mathbb{N}_0$ the linear functionals are the composition

$$\lambda_j := \delta_{\mathbf{x}^j} \circ D^{\boldsymbol{\eta}^j} \qquad \text{with} \quad |\boldsymbol{\eta}^j| \leq q. \tag{3.5}$$

The linear functionals are called pairwise distinct if for $j \neq k$ either $\mathbf{x}^j$ and $\mathbf{x}^k$ or $\boldsymbol{\eta}^j$ and $\boldsymbol{\eta}^k$ are pairwise distinct as well.

The translation invariant reproducing kernel Φ is now used to construct a native Hilbert space $\mathcal{H}_\Phi(\Omega)$ suited for the problem 3.1 and with its dual space containing the linear functionals λ_i as specified in Equation 3.5. Let $D_1^{\boldsymbol{\eta}}$ and $D_2^{\boldsymbol{\eta}}$ be the in 3.6.1. defined differential operator but regarding the first respectively second argument of a kernel $\Phi : \Omega \times \Omega \to \mathbb{R}$. Given a positive definite kernel $\Phi \in \mathcal{C}^{2q}(\Omega \times \Omega)$, the linear functionals $\lambda_j \in (\mathcal{H}_\Phi(\Omega))^*$ have

the according Riesz representers $\nu^j = D_2^{\boldsymbol{\eta}^j}\Phi(\cdot,\mathbf{x}^j) \in \mathcal{H}_\Phi(\Omega)$ for $j = 1,\dots,L$. The interpolant then takes the form $f = \sum_{i=1}^{L}\mu_i D_2^{\boldsymbol{\eta}^i}\Phi(\cdot,\mathbf{x}^i)$ by inserting the ν^j into equation (3.2). The parameters μ_i are computed by solving the linear equation system with interpolation matrix $A = \left(D_1^{\boldsymbol{\eta}^j} D_2^{\boldsymbol{\eta}^k}\Phi(\mathbf{x}^j,\mathbf{x}^k)\right)_{j,k=1}^{L}$ which is again invertible if the linear functionals are linear independent. For positive definite translation invariant $\Phi \in L_1(\mathbb{R}^n)\cap\mathcal{C}^{2q}(\mathbb{R}^n)$ holds: If the linear functionals $\lambda_j, j = 1,\dots,L$ as defined in Equation 3.5 are pairwise disjunct, they are also linear independent over $\mathcal{H}_\Phi(\mathbb{R}^n)$; cf. [10].

Now that the Hermite-Birkhoff concept is appropriately adapted, an obvious choice for the reproducing kernels are the radial basis functions. The following two examples provided by Wendland are shown to visualize the transition from translation invariant kernels mapped from two arguments to radial basis functions mapped from only one argument.

Examples 3.9. Subsequently, Φ denotes an on $\mathbb{R}^n$ translation invariant kernel.

1. Let $\mathcal{T}$ be a group of translations on $\mathbb{R}^n$. Choosing the transformation $T\boldsymbol{\xi} = \mathbf{x} - \boldsymbol{\xi}$ for fixed $\mathbf{x} \in \mathbb{R}^n$ implies $\Phi(\mathbf{x},\mathbf{y}) = \Phi(T\mathbf{x},T\mathbf{y}) = \Phi(\mathbf{0},\mathbf{x}-\mathbf{y}) =: \Phi_{\mathbf{0}}(\mathbf{x}-\mathbf{y}) =: \phi(\mathbf{x}-\mathbf{y})$, namely that a translational invariant Φ is equal to ϕ evaluated on the difference of Φ's two arguments.
2. Let $\mathcal{T}$ be a group of translations and orthogonal transformations on $\mathbb{R}^n$. Select the orthogonal transformation $U \in \mathbb{R}^{n\times n}$ for e_1 denoting the first unit vector of $\mathbb{R}^n$ with $U\xi = \|\boldsymbol{\xi}\|_2 e_1$. Then it follows that $\Phi(\mathbf{x},\mathbf{y}) = \Phi(U\mathbf{x},U\mathbf{y}) = \Phi_{\mathbf{0}}(U(\mathbf{x}-\mathbf{y})) = \phi(\|\mathbf{x}-\mathbf{y}\|_2 e_1) = \psi(\|\mathbf{x}-\mathbf{y}\|_2)$. Hence Φ is also radial.

Concludingly the radial basis functions are in fact radial, translation invariant kernels. Employing a positive definite RBF $\phi : \mathbb{R}^n \to \mathbb{R}$ with $\phi \in \mathcal{C}^{2q}(\mathbb{R}^n)\cap L_1(\mathbb{R}^n)$ for this concept induces a native Hilbert space $\mathcal{H}_\phi(\mathbb{R}^n) \subseteq \mathcal{C}^q(\mathbb{R}^n)$ ensuing the following characteristics:

1. For $|\boldsymbol{\eta}^j| \le q$ the linear functionals are continuous for all $\mathbf{x}^j \in \mathbb{R}^n$.
2. The to the linear functional λ_j according Rieszrepresenters are

$$\nu^j = (-1)^{|\boldsymbol{\eta}^j|}(D^{\boldsymbol{\eta}^j}\phi)(\cdot - \mathbf{x}^j), \qquad 1 \le j \le L. \tag{3.6}$$

3. The inner product is given by $\langle \nu^j, \nu^k\rangle_{\mathcal{H}_\phi(\mathbb{R}^n)} = (-1)^{|\boldsymbol{\eta}^k|}(D^{\boldsymbol{\eta}^j+\boldsymbol{\eta}^k}\phi)(\mathbf{x}^j - \mathbf{x}^k)$.

The factor $(-1)^{|\boldsymbol{\eta}^j|}$ appears here due to the differentiation regarding the second argument – refering to $D_2^{\boldsymbol{\eta}^j}$ – which is marked by the factor -1 in the argument of an translation invariant kernel respective RBF. Especially notable is the enormous flexibility of the Hermite-Birkhoff approach. Within this basement it is possible to select derivatives of different not successively increasing order as long as the requirements addressing $|\boldsymbol{\eta}^j|$ are fulfilled for all $j = 1,\dots,L$.

3.4 Space Augmentation

Compactly supported RBFs like the in Chapter 2 on page 4 presented Wendland's grant computational advantages since they lead to sparse interpolation matrices. Thus, they do

also create compactly supported interpolants and alas local methods applied to the interpolant "perceive" the function as zero everywhere apart from that local support. Therefore, an approach is needed that produces globally supported interpolants without relying on such a support in their basis functions.
One possible method to achieve this goal is to augment the space of interpolating functions with a suitable finite-dimensional function space $\mathcal{P}$, for example $\Pi_d(\mathbb{R}^n)$ – the space of polynomials on $\mathbb{R}^n$ whose degree is at most $d \in \mathbb{N}_0$. The so derived interpolant holds the additional property of reproducing elements of $\mathcal{P}$.
Let $\mathcal{P} \subset \bigcap_{i=1}^{L} dom(\lambda_i)$ be of dimension $m \in \mathbb{N}$ and let $\{p_1, \ldots, p_m\}$ be a basis for $\mathcal{P}$. Then, starting from the general concept in a Hilbert space $\mathcal{H}$ with the real dot product $\langle \cdot, \cdot \rangle_{\mathcal{H}}$, the augmented interpolant takes the form $f = \sum_{j=1}^{L} \mu_j \nu^j + \sum_{k=1}^{m} \gamma_k p_k$ with real coefficients γ_k added here.
Additionally, due to the reproducing property the first part of the interpolant f is orthogonal to all elements of $\mathcal{P}$. Thus, the condition

$$\sum_{j=1}^{L} \mu_j \lambda_j(p_k) = 0 \tag{3.7}$$

must hold for all $k \in \{1, \ldots, m\}$ and the only element from $\mathcal{P}$ annihilated by every linear functional λ_j is the zero-element from $\mathcal{P}$ itself.
Assembling the augmented interpolation conditions, one receives a linear equation system in the form of

$$\begin{pmatrix} \langle \nu^1, \nu^1 \rangle_{\mathcal{H}} & \ldots & \langle \nu^1, \nu^L \rangle_{\mathcal{H}} & \langle \nu^1, p_1 \rangle_{\mathcal{H}} & \ldots & \langle \nu^1, p_m \rangle_{\mathcal{H}} \\ \vdots & \ddots & \vdots & \vdots & \ddots & \vdots \\ \langle \nu^L, \nu^1 \rangle_{\mathcal{H}} & \ldots & \langle \nu^L, \nu^L \rangle_{\mathcal{H}} & \langle \nu^L, p_1 \rangle_{\mathcal{H}} & \ldots & \langle \nu^L, p_m \rangle_{\mathcal{H}} \\ \langle p_1, \nu^i \rangle_{\mathcal{H}} & \ldots & \langle p_1, \nu^L \rangle_{\mathcal{H}} & 0 & \ldots & 0 \\ \vdots & \ddots & \vdots & \vdots & \ddots & \vdots \\ \langle p_m, \nu^i \rangle_{\mathcal{H}} & \ldots & \langle p_m, \nu^L \rangle_{\mathcal{H}} & 0 & \ldots & 0 \end{pmatrix} \begin{pmatrix} \mu_1 \\ \vdots \\ \mu_L \\ \gamma_1 \\ \vdots \\ \gamma_m \end{pmatrix} = \begin{pmatrix} c_1 \\ \vdots \\ c_L \\ 0 \\ \vdots \\ 0 \end{pmatrix}$$

or with A defined as in Section 3.2 on page 8 and with $P = \left(\langle \nu^j, p_k \rangle_{\mathcal{H}}\right)_{\substack{j=1,\ldots,L \\ k=1,\ldots,m}}$ rougher expressed as

$$\begin{pmatrix} A & P \\ P^T & 0 \end{pmatrix} \begin{pmatrix} \boldsymbol{\mu} \\ \boldsymbol{\gamma} \end{pmatrix} = \begin{pmatrix} \mathbf{c} \\ \mathbf{0} \end{pmatrix}. \tag{3.8}$$

The lower part of the linear equation system (3.8) reflects the conditions (3.7). (3.8) is a symmetric indefinite linear equation system. Hence solving

$$\begin{aligned} (P^T A^{-1} P)\boldsymbol{\gamma} &= P^T A^{-1} \mathbf{c} \qquad \text{and} \\ A\boldsymbol{\mu} &= \mathbf{c} - P\boldsymbol{\gamma}, \end{aligned}$$

whereas $P^T A^{-1} P$ and A both are positive definite, is preferable; cf. [2].
Since the first part of f is orthogonal to any element of $\mathcal{P}$ it follows that data values $\mathbf{c}$ generated by an element $p \in \mathcal{P}$ will reproduce this very element as interpolant.

4

Interpolation for Modeling Implicitly Defined Surfaces

Simply said like Carr et al. explain it in [4]: "Cranioplasty is the procedure of repairing defects, usually holes, in the skull with cranial implants". Besides of the obvious reason – a scull defect due to an injuring accident – a craniectomy is performed on purpose e.g. in aim of reducing brain swelling (among various other medical indications to be read in [5]). This entails a cranioplasty for protection of the brain or bringing the patient's psychological disturbances at ease. Either the surgeon is sculpturing the bone implant manually directly after the removal or an implant is inserted in a subsequent operation involving high resolution computed tomography of the skull in its production (see [5] for more details). For the latter method a mathematical function is fitted to the CT data, and a computer numerically controlled mill is guiding the implant production via the reconstructed surface. The implant must serve an accurate model to secure a good fit. Since a restoration of the bone to a symmetrical skull will not always perform well, e.g. for resulting in large cavities between brain and implant, cf. [4], the surface has to be reconstructed through interpolation respectively approximation.

The framework presented in Chapter 3 allows now to be applied to such a graphical problem as the previous one presented. Given an object, like a cube, it is possible to set up data to describe that object's surface. In the paper [2] a point cloud with normal vectors belonging to each point are used to define that surface implicitly. In Figure 4.1 on the following page an example of those data belonging to an example cube can be seen used in Chapter 5 as well. The general concept presented in Chapter 3 is now used to reconstruct the surface of a three-dimensional object, so the spatial dimension n is now set to three.

4.1 Former Approaches to Surface Interpolation

Before pursuing the graphical example, a throwback shall elevate the elegance of the concept of [2] even more.

The method of using an implicit defined surface for reconstruction was already provided, e.g. described in [3] by Carr et al., resolving the issue of trivial zero-interpolants and hence the issue of surface orientation via the concept of "offset points". Offset points, namely, are not located on the surface, but shall softly indicate its boundaries. For a point $\mathbf{x} \in \mathbb{R}^3$ of the point cloud with associated normal $\mathbf{n}$, two offset points are constructed with a shaping

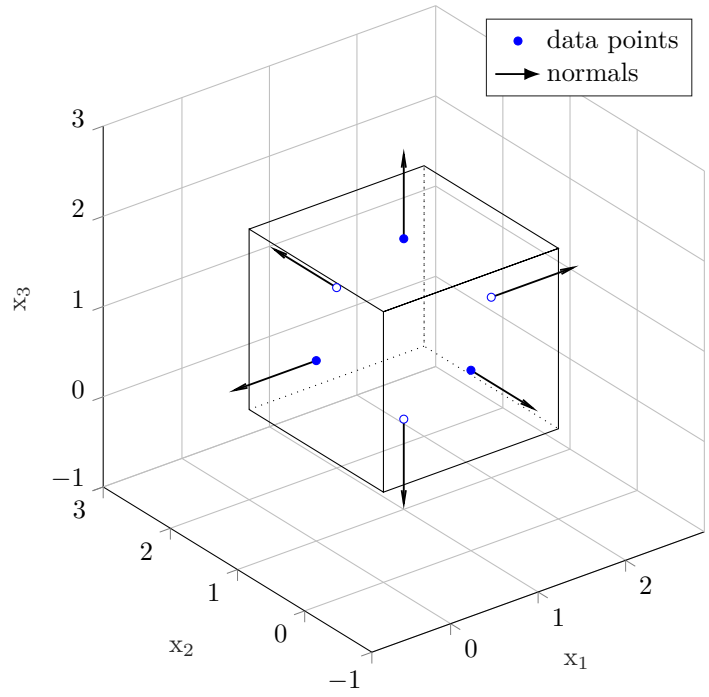

Figure 4.1: The surface of the cube – visualized in black edges – can be described through the points in $\mathbb{R}^3$ in the center of each face and normal vectors in $\mathbb{S}^2$ pointing outwards the surface from the data points.

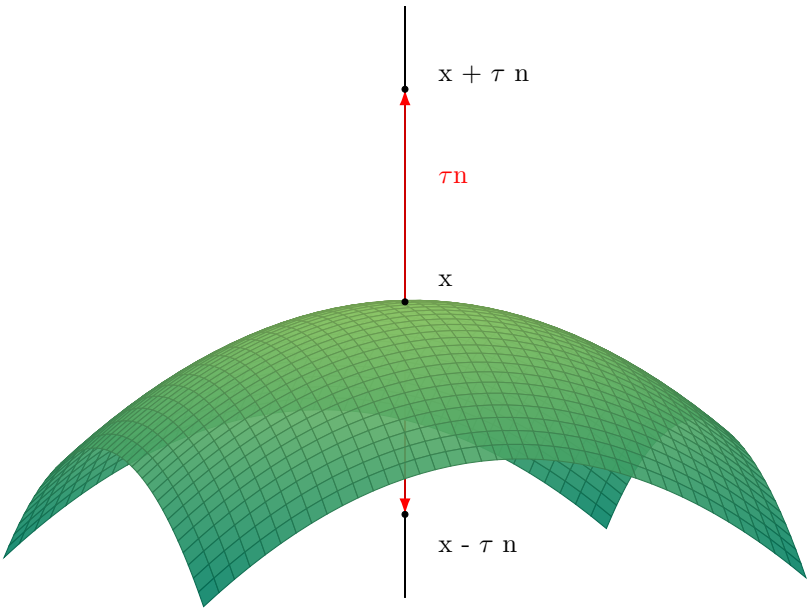

Figure 4.2: At the point $\mathbf{x} \in \mathbb{R}^3$ of the surface two offset points are constructed via $\mathbf{x} \pm \tau\mathbf{n}$ with $\tau > 0$. The offset points are projected from $\mathbf{x}$ along the normal vector $\mathbf{n}$ and shall indicate the surface's boundaries in the interpolation process.

parameter $\tau \in \mathbb{R}_{>0}$ in the form of $\mathbf{x} \pm \tau\mathbf{n}$ as visualized in Figure 4.2 on the previous page. This incorporates the surface normals, albeit not directly. The interpolants according to [3] and [2] carry positive values on the "outside" and negative values on the "inside" of the object's surface. Main issues of the offset points approach are the error-prone selection of τ and that the surface's orientation is not interpolated. Graphical visible advantages of the concept of Macêdo over this approach are also presented in [2].

4.2 Assembling the Interpolation Matrix and Interpolant

The surface of the object will be modeled through an implicit function, so to say a function which is set to zero at every point included in the object's surface. Therefore, the fact can be employed that the gradient – defined as column vector – of the function defining an implicit surface accords to the normal vector at the same point. For simplification it will be assumed that each $\mathbf{x}^l$ in the set of pairwise distinct nodes $\{\mathbf{x}^l \in \mathbb{R}^n, l = 1, \dots, N \in \mathbb{N} \mid \mathbf{x}^j \neq \mathbf{x}^k \text{ for } j \neq k\}$ is assigned to one linear functional with $|\boldsymbol{\gamma}^{i_1}| = 0$ and to three linear functionals with $|\boldsymbol{\gamma}^{i_k}| = 1, k = 2, 3, 4$. Hence the problem shapes as follows:

Problem 4.1. Given a data set $\{\mathbf{x}^1, ..., \mathbf{x}^N\} \subseteq \mathbb{R}^3$ for $N \in \mathbb{N}$ and corresponding normal vectors $\{\mathbf{n}^1, ..., \mathbf{n}^N\} \subseteq \mathbb{S}^2$, the aim is to find a function $f : \mathbb{R}^3 \to \mathbb{R}$ that fulfills

$$f(\mathbf{x}^i) = 0 \qquad \text{and} \tag{4.1}$$

$$\nabla f(\mathbf{x}^i) = \mathbf{n}^i \tag{4.2}$$

for all $i = 1, ..., N$ and with $\nabla f = (\partial_1 f, \partial_2 f, \partial_3 f)^T$.

Therefore, one obtains $L = 4N$ linear functionals and the Riesz representers of the linear functionals are N times the evaluation of the RBF at each difference combination among the points and $3N$ times the RBF's first derivative regarding each coefficient of the RBF's centers. Equally the data vector $\mathbf{c} \in \mathbb{R}^{4N}$ contains N entries with 0 and $3N$ entries filled with to the linear functionals corresponding normal vectors. Considering that $|\boldsymbol{\eta}^i|, i \in \{1, \dots, L\}$ is at most 1, the use of positive definite $\phi \in \mathcal{C}^2(\mathbb{R}^3)$ is required.
Let ∇f be defined as in problem 4.1 and $H = (\partial_{j,k})_{j,k\in\{1,2\}}$ denote the Hess matrix operator. Concludingly, by inserting $f = \sum_{k=1}^{4N} \mu_k \nu^k$ with Riesz representers ν^k from Eq. (3.6) into the Equations (4.1) and (4.2) the following equations, with $\boldsymbol{\mu}$ consisting of the $\alpha_i \in \mathbb{R}$ and $\boldsymbol{\beta}^i \in \mathbb{R}^3$ for $i \in \{1, ..., N\}$, are delivered in the form

$$0 = \sum_{k=1}^{N} \alpha_k \phi(\mathbf{x}^i - \mathbf{x}^k) - (\nabla\phi\ (\mathbf{x}^i - \mathbf{x}^k))^T \boldsymbol{\beta}^k \tag{4.3}$$

$$\mathbf{n}^i = \sum_{k=1}^{N} \alpha_k \nabla\phi\ (\mathbf{x}^i - \mathbf{x}^k) - H\phi\ (\mathbf{x}^i - \mathbf{x}^k)\ \boldsymbol{\beta}^k \tag{4.4}$$

and the interpolation matrix has the structure

$$A = \begin{pmatrix} \overbrace{\phi(\mathbf{x}^j - \mathbf{x}^k))_{j,k=1}^N}^{\in\mathbb{R}^{N\times N}} & \overbrace{((-\nabla\phi(\mathbf{x}^j - \mathbf{x}^k))_{j,k=1}^N)^T}^{\in\mathbb{R}^{N\times 3N}} \\ \underbrace{(\nabla\phi(\mathbf{x}^j - \mathbf{x}^k))_{j,k=1}^N}_{\in\mathbb{R}^{3N\times N}} & \underbrace{(-H\phi(\mathbf{x}^j - \mathbf{x}^k))_{j,k=1}^N}_{\in\mathbb{R}^{3N\times 3N}} \end{pmatrix}.$$

The vectors $\mathbf{c}$ and $\boldsymbol{\mu}$ are to be filled with zeros and normals respectively α_i and $\boldsymbol{\beta}_i$ parts according to the structure of A in concordance with equations (4.3) and (4.4). The interpolant then concludes as

$$f(\mathbf{x}) = \sum_{i=1}^{N} \left(\alpha_i \ \phi(\mathbf{x} - \mathbf{x}^i) - \langle \boldsymbol{\beta}^i, \nabla\phi(\mathbf{x} - \mathbf{x}^i)\rangle_{\mathbb{R}^3}\right). \tag{4.5}$$

Remark 4.2. In the next chapter some graphical experiments were implemented using the in example 2.3 on page 4 defined Gaussian and Wendland RBFs. Differentiating the Wendland RBF $\phi_\varepsilon(\mathbf{x})$ for the second time, a disturbing term including the norm of $\mathbf{x}$ as divisor appears. For computation this point of discontinuity is replaced by its limit.

Augmenting $\mathcal{H}_\phi(\mathbb{R}^3)$ with the space $\Pi_d(\mathbb{R}^3)$, the linear equation system with $p_j := (p_j(\mathbf{x}^1), \ldots, p_j(\mathbf{x}^N)) \in \mathbb{R}^{1\times N}$ representing again the basis for polynomials takes the form

$$\begin{pmatrix} & \mathrm{A} & & (p_j)_{1\le j\le m} \\ & & & (\nabla p_j)_{1\le j\le m} \\ (p_j)_{1\le j\le m} & (\nabla p_j^T)_{1\le j\le m} & & 0 \end{pmatrix} \begin{pmatrix} \boldsymbol{\alpha} \\ \boldsymbol{\beta} \\ \boldsymbol{\gamma} \end{pmatrix} = \begin{pmatrix} \mathbf{0} \\ \mathbf{n} \\ \mathbf{0} \end{pmatrix}.$$

The single subindex j indicates the rows of a submatrix here.
Adding up the linear combination of the polynomial basis with the coefficients contained in $\boldsymbol{\gamma} \in \mathbb{R}^m$ to the interpolant generates the augmented interpolant that is also capable of reproducing any polynomial of maximum degree $d \in \mathbb{N}_0$.

4.3 Surface Interpolation and Raytracing

The collocation of the interpolation set-up for the surface reconstruction is already completed. This just leaves a technical comment here on the advantage of an implicit representation of surfaces which seems a little bit laborious to work with regarding the rendering of objects in a scene. The quality of the surface's implicit representation expressed through a mathematical function is its compatibility with raytracing. Equipping a scene to be shown in an image with realistic optical features – such as lighting, shadowing, reflection, refraction etc. – rays are sent through the scene to be mapped and intersection points are calculated for tracing the interaction of the light rays with the objects in the scene. A mathematical representation of the surface helps with these intersection calculations regarding a ray R. This ray can be represented e.g. by an origin vector $\vec{o}$ and a direction vector $\vec{d}$ in the form $R(t) = \vec{o} + t\vec{d}, t \ge 0$, and its intersection with the surface can be calculated by finding the minimal nonnegative parameter t for which the equation $f(R(t)) = 0$ holds.

5

RESULTS

Although the implicit splines are normally used for surface interpolation on coarse data it was chosen to study a simple surface on the contrary to demonstrate characteristics of the Gaussian RBF and Wendland's RBF in the approach in [2]. As sub-criteria each RBF is applied to the same two data sets describing two simple solids. In this chapter the unindexed x, y, z denote the first to third component of the points in $\mathbb{R}^3$.

5.1
Surface Reconstruction with Gaussian Radial Basis Functions

To get started on this graphical application, a simple object to be reconstructed was chosen – a cube. A cube consists of six even surfaces and has sharp edges which were also the characteristics studied primarily. Beginning with Gaussian RBFs for the experiments in Figure 5.1 on the next page one can see the reconstruction of a cube with the interpolation concept from Chapter 3 for different shaping parameters ε. The subplots from each plot show a comparison of edges in side view between the approximated cube and an ideal cube – represented by the black framed sqare. It can be discovered that by increasing ε, the approximated cube fills in to the form of an ideal cube with growing congruence, finally actually inverting its curvature. At higher ε the function forms sphere-like bumps at the corners and dents in the plane centers.

To exclude any bias due to the normal vectors oriented parallel to the coordinate axes, the same cubes were also approximated on rotated data with the results captured in Figure 5.2. Clearly evident the rotation has no effect on neither of the graphical ε-Extrema.

Dedicating the next graphic to the space augmentation with polynomials the same cube with an $\varepsilon = 2.0$ is presented with increasing polynomial degree from the left to the right. Focusing on the influence of that degree in Figure 5.3 on page 20 there is a swelling smoothing of edges and cube corners noticeable. Augmenting the interpolant space with $\Pi_2(\mathbb{R}^3)$ results in a spherical surface illustrated at the right of Figure 5.3.
Interpreting ε as energy for the multidimensional splines the Gaussian RBF based interpolant prefers sphere-like surfaces for low energy and plane surfaces for higher energy. This characteristic also persists in the interpolant on the rotated data excluding any bias due to spatial orientation of the data. Augmenting the interpolant space with polynomials of degree d the polynomial influence excels in a rounding of edges and corners. For $d \geq 2$ the dimension of $\Pi_d(\mathbb{R}^3)$ overruns N in this cube example and hence dominates the Gaussian RBF characteristics which can be seen in the spherical appearance of the interpolated sur-

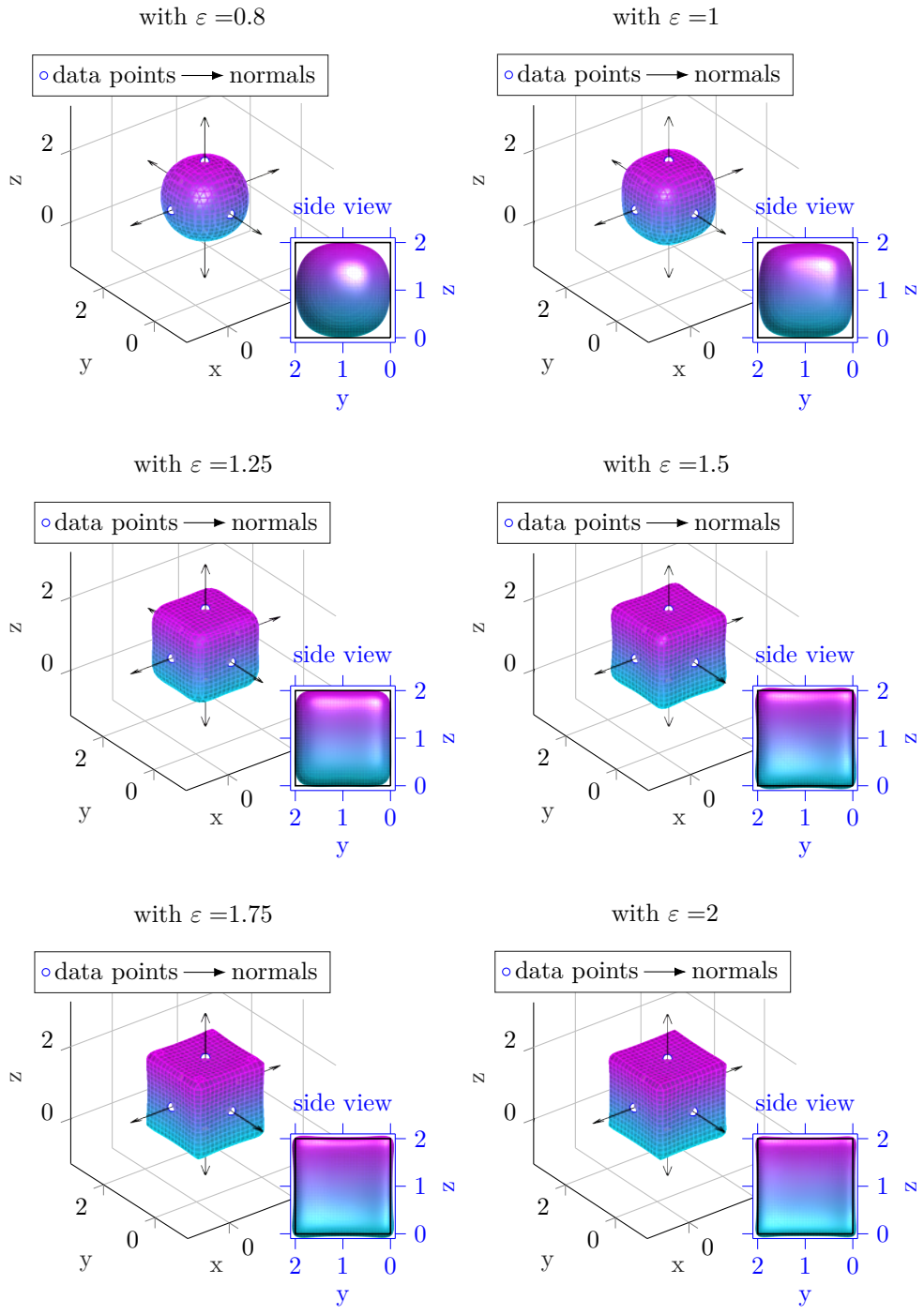

FIGURE 5.1: A cube's surface reconstructed with Gaussian RBFs on the data illustrated in Figure 4.1 show that the cube's faces appear spherical for lower and more planar for higher ε. The subplots show an edge comparison of the reconstructed with the ideal cube (black edges) in side view and indicate that the surfaces curvature inverts its direction from outside to inside for growing ε.

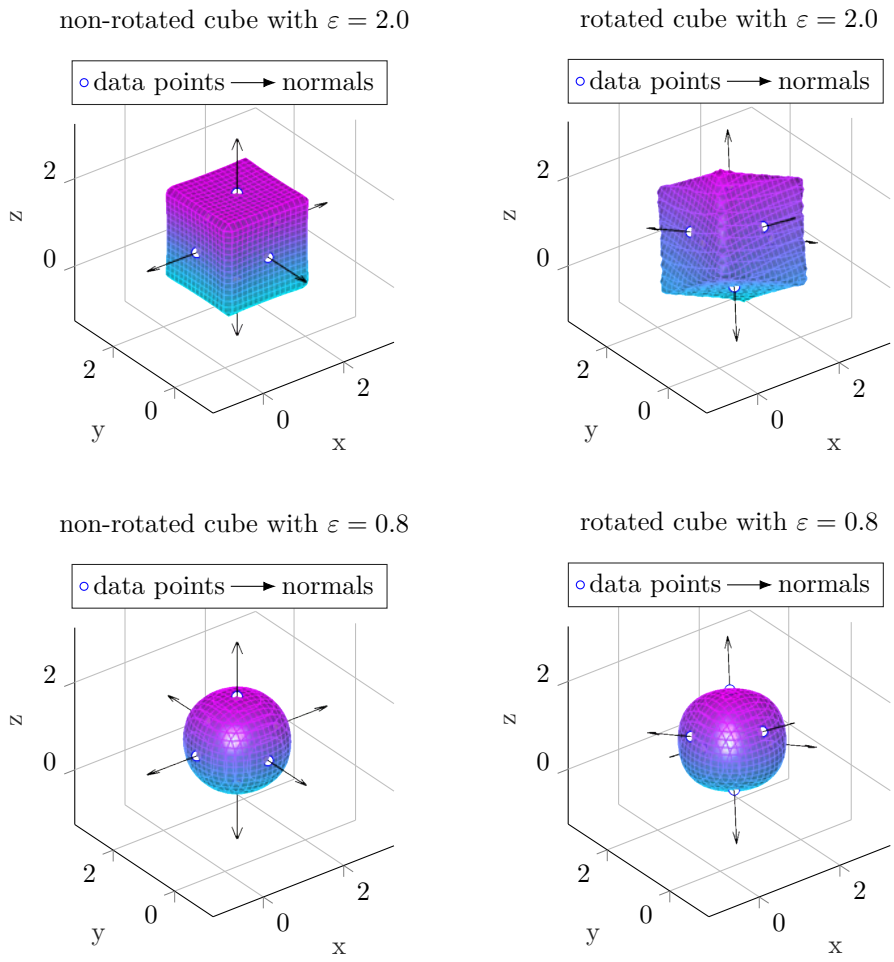

FIGURE 5.2: The left column of plots shows the with Gaussian RBFs reconstructed cubes for two graphical "extreme" values of shaping parameter: $\varepsilon = 2.0$ results in a planar and $\varepsilon = 0.8$ in a sphere-like surface. Rotating the data by 40° around the axis $(-3, 2, 0)^T$ does not effect the surface except for it's spatial alignment.

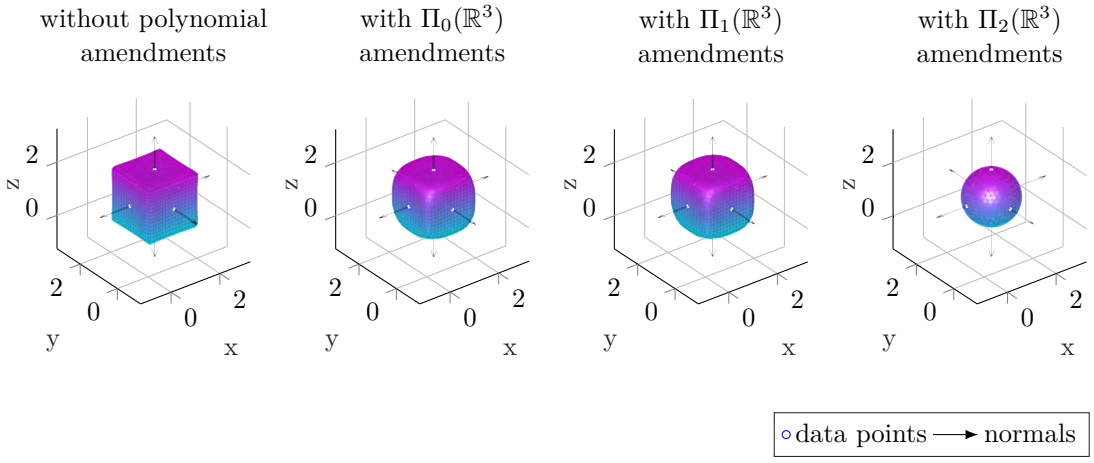

FIGURE 5.3: The interpolation of cubes (Gaussian RBFs) with $\varepsilon = 2.0$ and increasing degree in polynomial amendments results in a smoothing of edges and a dulling of corners in the cube's surface, till the polynomial term in the interpolant prevails in the surfacs's appearance for $d = 2$.

face on the right of Figure 5.3.
Descending one step further on the scale of simplicity regarding the geometric solid to be reconstructed, a regular tetrahedron was studied next. The number of faces decreases to 4, but systematically the same kind of data were constructed as in Figure 4.1 on page 14 – points in the center of each face with related normals from the 2-sphere $\mathbb{S}^2$. The key difference to the cube are the pointier corners which place an observable quality of the interpolant. The same observations can be made on the tetrahedra as with the cubes for increasing ε (even though ε in this case is ranging from 1.0 *(spherical)* to 8.0 *(planar)*) and also the rotational invariance is fulfilled – both plotted in Figure 5.4 on the following page. Here the left column shows the "untouched" tetrahedron for $\varepsilon = 3.0$ – a transitional value between the two optical extrema – and the upper value $\varepsilon = 8.0$. The right column shows the same tetrahedra on rotated data with rotation parameters like in Figure 5.2 on the previous page and were added into the graphic for a better view on the tetrahedra respectively to demonstrate the rotational invariance. The independence of the data also persists for the interpolant augmentation with polynomial terms. In particular the smaller angle of a triangle reveals the corner denting effect of the $\Pi_0(\mathbb{R}^3)$ polynomials even more as shown for $\varepsilon = 8.0$ in Figure 5.5. Augmenting the tetrahedron with any higher degree than $d = 1$ is again not reasonable in this particular case since the dimension m of the polynomial space outpaces the number of data points N and therefore dominates the graphic. The surface keeps still interpolating the datapoints for those higher degrees d but takes rather the implicit forms of the polynomials themselves. Looking at the coefficients it can also be observed that the weight of the interpolation data decreases with growing polynomial degree. Since scattered data interpolation mostly works with large data sets; this concern shall not bother any further but simply gets acknowledged.

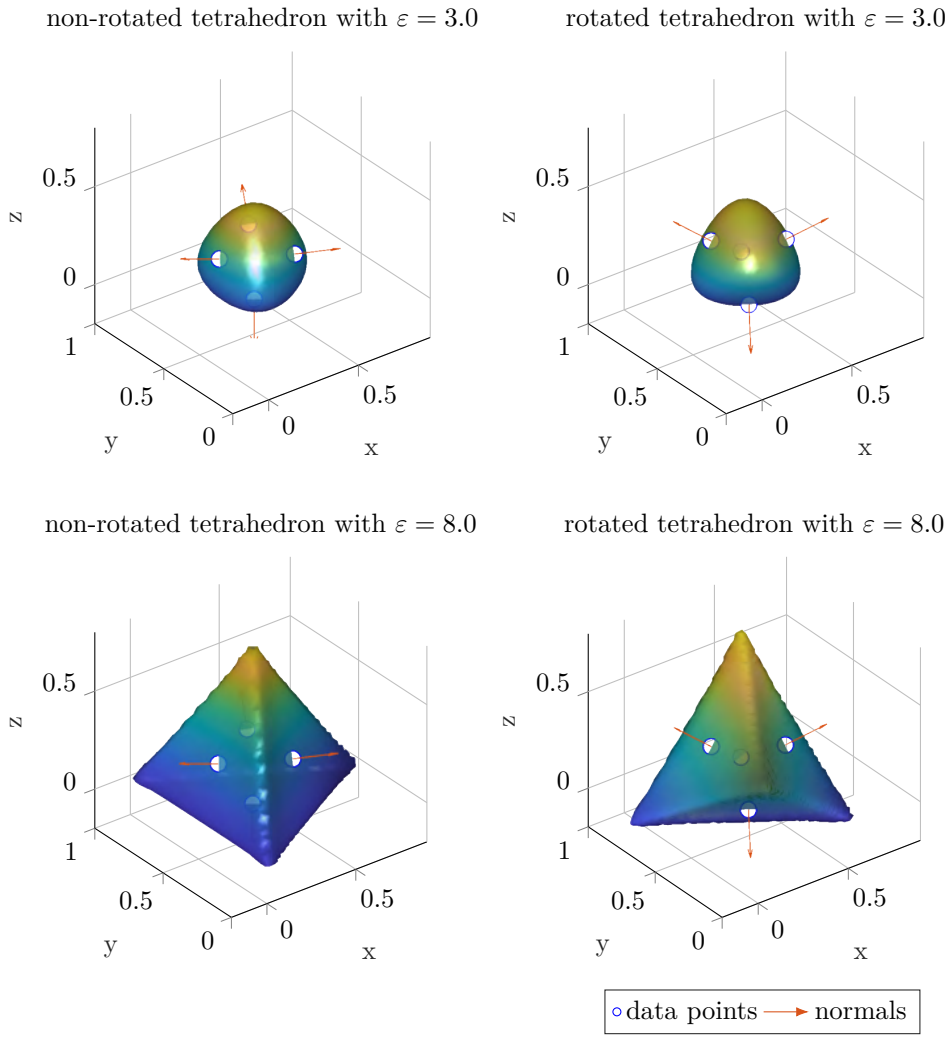

FIGURE 5.4: With Gaussian RBF reconstructed tetrahedra for $\varepsilon = 3.0$ in the first and $\varepsilon = 8.0$ in the second row show rotational invariance in the second column, where the data are rotated by 40° around the axis $(-3, 2, 0)^T$.

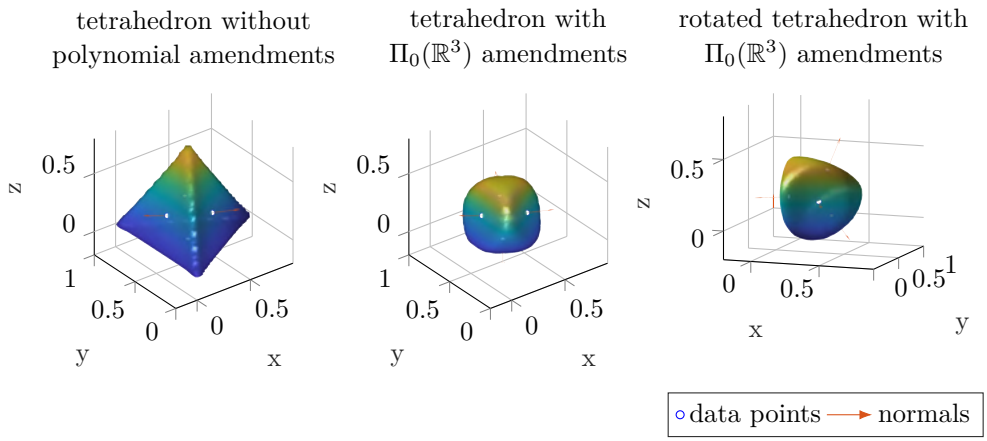

FIGURE 5.5: The with Gaussian RBF reconstructed tetrahedron with $\varepsilon = 8.0$ in the left plot and additional polynomial amendments of $\Pi_0(\mathbb{R}^3)$ on the right confirm the edge smoothing and corner denting effect of polynomial augmentation observed in Figure 5.3.

5.2
Surface Reconstruction with Wendland's Radial Basis Functions

Departing now from the Gaussian RBF, center of attention in this second part lies on the compactly supported Wendland RBF ϕ_ε with associated radial function $\psi_{3,1}$ as defined in example 2.3 of the second chapter. Here in Figure 5.6 an example in [10] was successfully reproduced which initially triggered the idea to focus on the influence of the shaping parameter ε in the modeling of simple solids. What Macêdo et al. conceal in their graphic and hence was also concealed in Figure 5.6 are the "isosurfacing artifacts" as Macêdo calls them. Fathoming in the following what those isosurfacing artifacts are the return to the roots – the Wendlands' themselves – is necessary first. In example 2.3 on page 4 the Wendland functions $\psi_{3,1}$ were characterized with compact support in $[0, 1] \subseteq \mathbb{R}$ which can be scaled through the shaping parameter ε representing the support radius. Because the RBF evaluates this function on the Euclidean norm, the compact support is now bounded to the closed unit ball respectively scaled through ε. Now, what are isosurfacing artifacts exactly: Zeros outside the aggregation of ε-scaled unit balls around the data sites, i.e. $\bigcup_{i=1}^{N} \overline{B_\varepsilon(\mathbf{x}^i)}$ with $\overline{B_\varepsilon(\mathbf{x}^i)} := \{\mathbf{x} \in \mathbb{R}^3 : \|\mathbf{x} - \mathbf{x}^i\| \leq \varepsilon\}$, that do not actually belong to the reconstructed surface. The area of artifacts can be described as a form of the support's inherited complement. The only surface's real zeros are on transitional points between the positive and negative support subsets in $\bigcup_{i=1}^{N} \overline{B_\varepsilon(\mathbf{x}^i)}$. Positive and negative support subsets refer to the subsets of $\bigcup_{i=1}^{N} \overline{B_\varepsilon(\mathbf{x}^i)}$ that are mapped to positive respectively negative values. In Figure 5.7 the blunt artifacts are partwise visible. Partwise alludes to the fact that the artifacts are actually the ubiquitous nonvisible part since the plotted surfaces in Figure 5.7 only represent boundary surfaces to the interpolant's support. It might seem quite irritating that the support takes the form of a bisected ball for $\varepsilon = 0.5$. Admittedly this is due to the

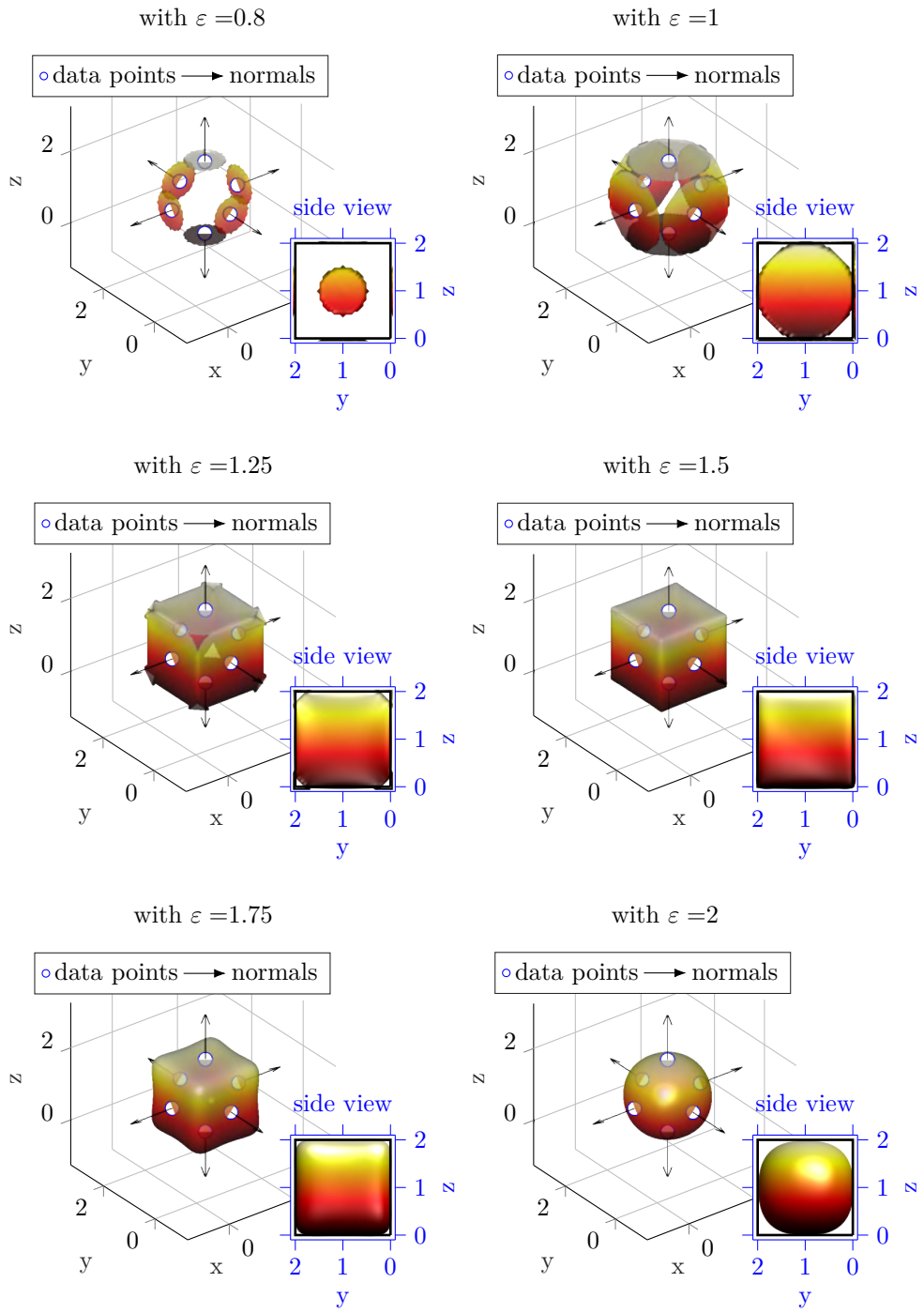

FIGURE 5.6: The interpolation approach on the cube data as depicted in Figure 4.1, with Wendland RBF ϕ_ε ranging ε from 0.5 to 4, shows six disjoint disks that approach each other and finally melt to the cube's surface for growing radius $\varepsilon > 0$.

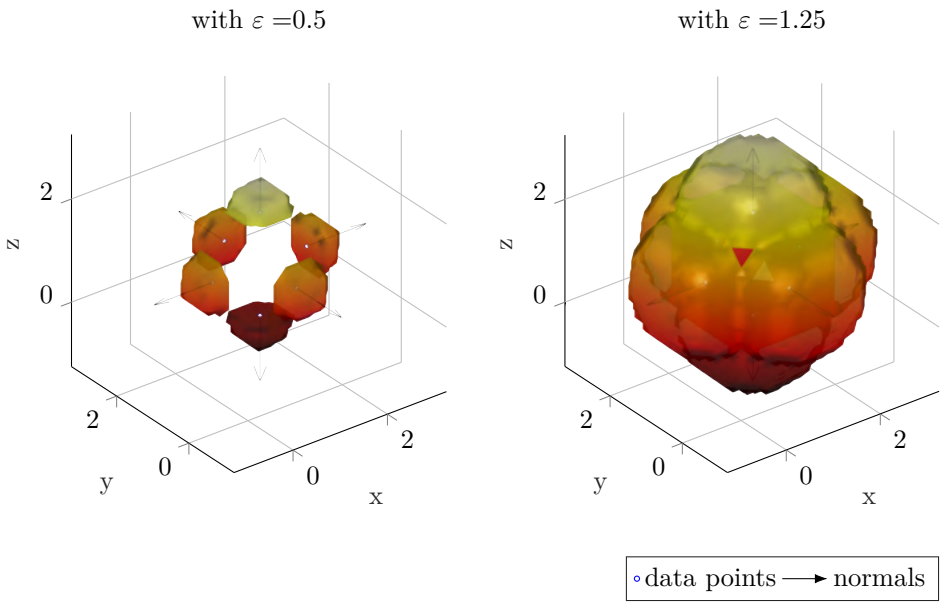

FIGURE 5.7: The cube's surface function interpolated with the Wendland RBF carries non proper zeros that are inherited by the Wendland's compact support and are depicted here as boundary surface to positive values of the interpolant in the outstanding bulges for radius $\varepsilon = 0.5$ and $\varepsilon = 1.25$.

slight positive approximation of the zero which is equaled to the function for evaluating the surface. It was left this way in graphic 5.7 to have a better sight on the cube's reconstructed faces. A contour plot for the level $z = 1$ in Figure 5.8 on the next page shows that the corresponding negative support subsets really do exist which could be graphically confirmed by implicitly plotting the negative interpolant $-f$ along with the original one. The zero contours separating the positive from the negative support subsets are the modeled parts of the cube's faces visible in graphic 5.6 on the preceding page.
Whereas these artifacts might cause repulse in the field of computer graphics their evolution for growing ε is actually quite fascinating and soothing to look at. Therefore, in Figure 5.9 the transition of artifact borders with growing ε is depicted, but the domain is restricted on a distance of 0.5 to the cube in each axis direction individually to have a glance into the positive support subset and the hereby evolving cube itself. One can observe that as the disjoint disks on the cube faces draw nearer to one another, the borders to the artifact area do likewise until the parts of both simultaneously start individually to melt together to a continuous surface and the artifacts dissolve from the inner cube.

A solution for resolving the artifact issue is as motivated in Section 3.4 the interpolant space augmentation with polynomials effectively, demonstrated in Figure 5.10

. However the polynomial amendments did not have an artifact diminishing effect until the cube's planes were closed completely, i.e. for $\varepsilon < \sqrt{2}$, as long as the polynomials did not prevail (for $d < 2$).

In the cube example the choice of the plane's circumcircle respectively the maximum of the minimal distance from a data point $\mathbf{x}^i$ to another point is optimal. To test this thesis for another symmetrical solid the polynomial degree dependent interpolant in Figure 5.11

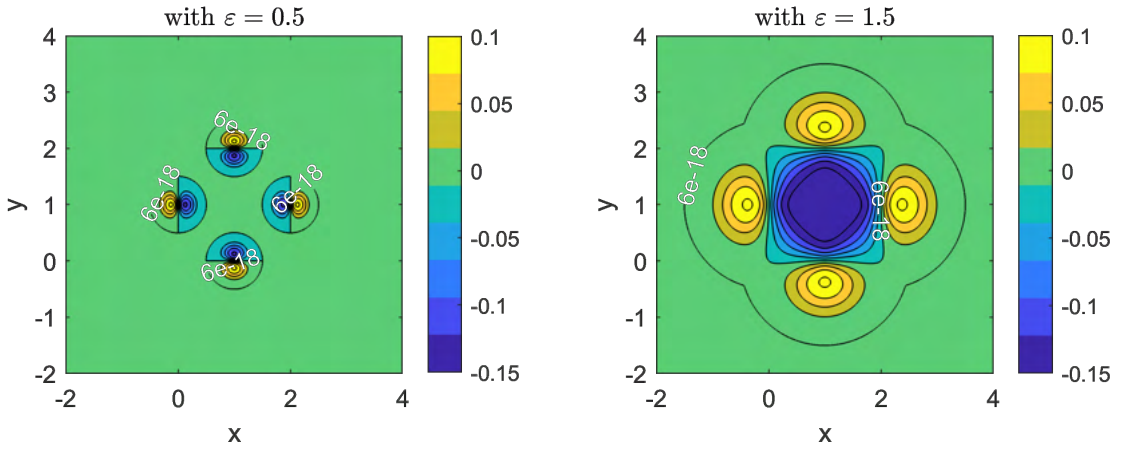

FIGURE 5.8: The contour plots show the Wendland RBF cube's surface function at $z = 1$. The (outer) $6e-18$ level indicates the transition line from the isosurfacing artifacts (0 level outside) to positive codomain. The artifacts' surface transitioning into negative codomain is also existent for $\varepsilon = 0.5$ but vanishes for higher ε. The white area within the $\varepsilon = 1.5$ contour-plot only contains lower function levels not displayed here.

demonstrates on the tetrahedron that a radius of $\varepsilon = \frac{\sqrt{3}}{3}$ is sufficient for eliminating the isosurfacing artifacts by polynomial augmentation. The reason why the artifacts are not visible in Figure 5.11 is that here the negative interpolant $-f$ was plotted to highlight the pointy corners using Wendland RBFs in comparison to the Gaussian in Figure 5.5. Sadly, the corner denting phenomena detected on the Tetrahedron reconstructed with Gaussians does not spare the Tetrahedron in Figure 5.11 either.

5.3 Comparing Radial Basis Functions In Surface Interpolation

After this examination of the selected RBFs' influence on the surface interpolation of the two simple geometric solids, certain characteristics can be deduced for the RBFs individually and as representative examples for compactly respective non-compactly supported radial basis functions. The Gaussian RBFs prefer spherical surfaces for lower and planar faces for higher energy alias the shaping parameter ε. The other way around Wendland RBFs present disjunct disks for smaller ε and sphere-like surfaces for higher ε, whereby the shaping parameter here is not interpreted as energy but as radius of the locally determined surface around a data side. Therefore, the shaping parameters of the Gaussian and Wendland RBF do not belong to the same category. The radius of the Gaussian is infinite since they are globally supported. Then again, for the Wendland RBF a change of curvature does in some way correlate the radius size, as visible in the graphic 2.2 on page 7 displaying the

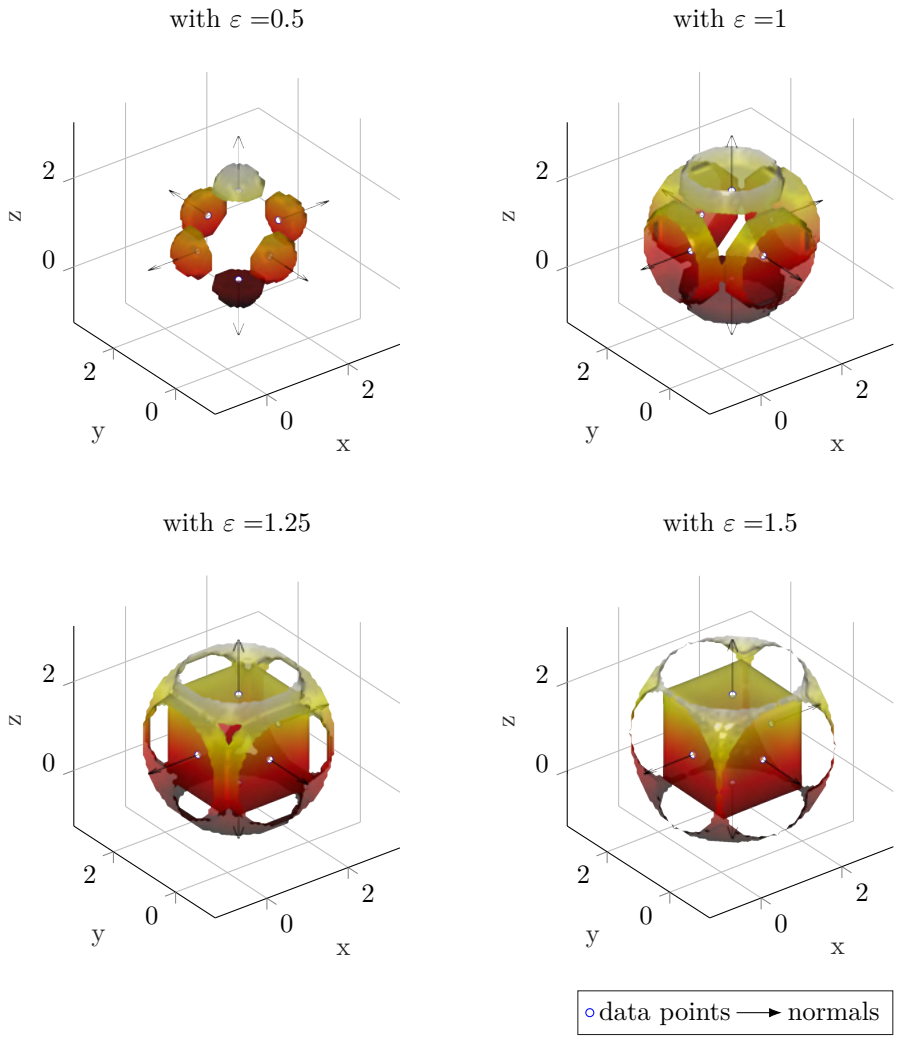

FIGURE 5.9: The outer artifacts' surfaces on the Wendland RBF cube grow with the cube's displayed faces and dissolve from them with increasing ε ranging from 0.5 to 1.5 from the left to the right.

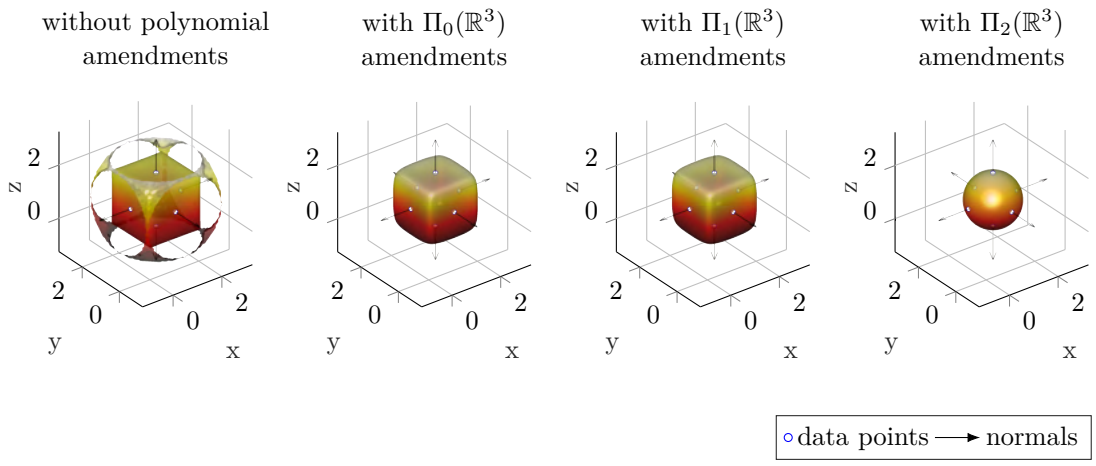

FIGURE 5.10: The artifact's surfaces from the Wendland RBF cube with $\varepsilon = \sqrt{2}$ disappear by augmenting the interpolant with terms from $\Pi_d(\mathbb{R}^3), d = 0, 1, 2$.

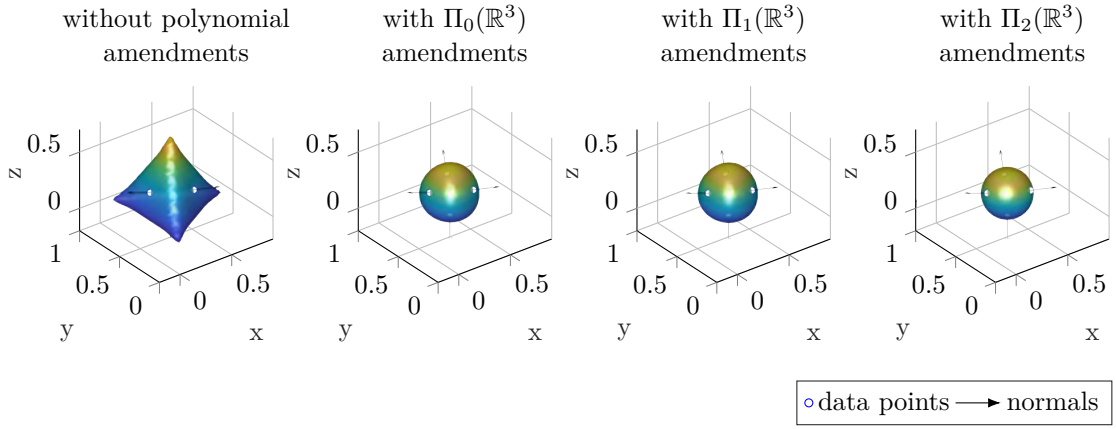

FIGURE 5.11: The tetrahedron data interpolated with Wendland RBF and $\varepsilon = \frac{\sqrt{3}}{3}$ are also effected by the space augmentation with $\Pi_d(\mathbb{R}^3), d = \{0, 1, 2\}$, displaying in the three plots on the right the corner denting phenomena from Figure 5.3 in comparison to the one left plot without polynomial amendments.

Wendland RBF on $\mathbb{R}^2$. But the curvature can also be tuned by the degree of smoothness $2q$ for the radial function $\psi_{3,q}$. Through the sparsity the interpolation matrix with Wendland RBFs possesses a smaller condition, but then again needs the interpolant space augmentation with at least $\Pi_0(\mathbb{R}^3)$ to eradicate the isosurfacing artifacts. Those artifacts display in the inherited support's complement of the Wendland RBFs with datapoints $\mathbf{x}^i,\ 1 \leq i \leq N$, in the center each. The rotational invariance could successfully be confirmed for the interpolation process with each RBF and a dullness on the corners and rounding of edges could be detected through polynomial amendments for both RBFs regarding the cube and the tetrahedron example.
The matter of dealing with close sheets was not studied here, but Macêdo et al. demonstrated in numerous graphics in [2] how powerful the Hermite radial basis function implicits can be. In their surfaces working with polynomial augmentation a smoothing can be determined as well on their larger nonsymmetric data sets working with Wendland's RBFs.

6

Conclusion and Outlook

Starting with the optimal recovery problem in Section 3.1 on page 8, an abstract solution of the norm optimal interpolant is delivered through the linear combination of the Riesz representers. Those represent the linearly independent linear functionals of a Hilbert space's continuous dual space that are to be interpolated. The existence of such Riesz representers is guaranteed by the Riesz representation theorem. It is proven by Wendland that this interpolant solution really holds the norm optimality as outlined in proof 3.2. Narrowing this down to linear functionals taking the form of a composition of an evaluation functional with a differential operator the flexible concept of Hermite-Birkhoff interpolation evolves. Most notable is that as long as the linear functionals in Hermite-Birkhoff are pairwise distinct they are also linearly independent. Hermite-Birkhoff relies on positive definite translation-invariant kernels which can be represented by positive definite radial basis functions since RBFs hold in fact the properties of radial translation invariant kernels. Thus, positive definite radial basis functions fulfilling the conditions of smoothness, i.e. $\phi \in \mathcal{C}^{2q}(\mathbb{R}^n)$, can be incorporated into the interpolation concept. As an add-up the by the kernels induced native Hilbert space can be augmented by a finite-dimensional function space whereby the retrieved interpolant holds the reproducing property in the sense that it reproduces elements of the augmenting function space. For this additional tool the space of polynomials on $\mathbb{R}^n$ with degree at most d was chosen. Applying the concept with RBFs to geometric modeling yields simple algorithms with directly translated mathematics. Twice continuously differentiable RBFs suffice to interpolate point clouds with associated normal vectors from the unit 2-sphere which represent the implicit function's gradients. With an the amount of data points N the symmetric interpolation matrix has full rank $4N$ and is sparse for the use of the compactly supported Wendland RBFs resulting in much more efficient computation. But this is not a topic here since only small data sets were studied in this thesis. On the other hand, relying on the globally supported Gaussian RBFs proves better extrapolating qualities. The latter RBFs show a stronger curvature for lower shaping parameter and rather planar appearance in the surfaces for higher ε. The Wendland RBF's compact support is scaled by the radius respectively shaping parameter and translates in some form to the interpolation site. Its complement gets inherited from the RBFs by the interpolant and therefore isosurfacing artifacts arise outside the union of ε-scaled unit balls around the data points. The isosurfacing artifacts vanish by augmenting the interpolant with polynomials of minimum degree zero as soon as the object's proper surface is closed, but the value of the minimum radius necessary for that was not discussed. Polynomial augmentation in general results in a smoothening of the object's surface which confirms the observations of Macêdo

in [2]. For the dimension of the selected polynomial space outranging the amount of data points the polynomial term prevailed in the surface while still interpolating the data points and normals. The rotational invariance which persists in the approach of [2] due to the rotational invariance of the norm respectively the RBFs could be observed in the graphics as well.

Pursuing this work, it would be interesting to exploit the Hermite-Birkhoff flexibility in the graphical application further. Starting in general by observing the interpolating behavior of curvature matrices one might hereafter focus e.g. on the performance on surface reconstruction when leaving out the surface point's zero value just relying on the normal there or dropping even the normal and just interpolating the curvature together with the zero value. Additionally, the locality property mentioned by Wendland regarding his compactly supported RBFs could prepare the way for increasing the efficiency in surface computation even more as long as one does not choose the support radius enclosing all data points like Macêdo et al. did in [2].

Leaving the application of geometric modeling but staying in the field of imaging, the interpolation approach might suit a problem from image registration. This field deals with finding optimal geometric transformation between corresponding image data; cf. [6]. Creating an interpolant mapping two coordinates to their transformed ones, it is simply required solving one linear equation system for each coordinate coefficient dealing with the same interpolation matrix for both. Furthermore, the framework can be utilized for several other problems where interpolation of scattered data is helpful.

Bibliography

[1] Haykin, S. *Neural Networks and Learning Machines*. Third Edition. Pearson Education, 2009.

[2] I. Macêdo J. P. Gois, L. V. Hermite Radial Basis Functions Implicits. In: *Computer Graphics Forum* 0(0):1–16, 2010.

[3] J. C. Carr R. K. Beatson, J. B. C. *Reconstruction and Representation of 3D Objects with Radial Basis Functions*. 2001.

[4] J. C. Carr W. R. Fright, R. K. B. Surface Interpolation with Radial Basis Functions for Medical Imaging. In: *IEEE TRANSACTIONS ON MEDICAL IMAGING* 16(1), 1997.

[5] L. Rauschenbach C. Rieß, U. S. Personalized Calvarial Reconstruction in Neurosurgery. In: *Towards the Automatization of Cranial Implant Design in Cranioplasty II*. First Edition. Springer Nature Switzerland, 2021, pp. 1–7.

[6] Modersitzki, J. *Numerical Methods For Image Registration*. Numerical Mathematics and Scientific Computation. Oxford University Press, 2004.

[7] Opfer, G. *Numerische Mathematik für Anfänger*. Fifth Edition. Vieweg & Teubner, 2008.

[8] PAN R. MENG X., W. T. Hermite variational implicit surface reconstruction. In: Science in China Series F: Information Science, 2009.

[9] Wendland, H. Piecewise polynomial, positive definite and compactly supported radial functions of minimal degree. In: *Advances in Computational Mathematics* 4:389–396, 1995.

[10] Wendland, H. *Scattered Data Approximation*. First edition. Camebridge University Press, 2005.

[11] Wendland, H. Computational Aspects of Radial Basis Function Approximation. In: *Topics in Multivariate Approximation and Interpolation*. Vol. 12. Studies in Computational Mathematics. Elsevier, 2006, pp. 231–256.